Available online at www.sciencedirect.com

SciVerse ScienceDirect

Acta Materialia 61 (2013) 1921–1931

Acta MATERIALIA

www.elsevier.com/locate/actamat

A thermoplastic forming map of a Zr-based bulk metallic glass

N. Li [a], Y. Chen [b], M.Q. Jiang [b], D.J. Li [a], J.J. He [a], Y. Wu [c], L. Liu [a,*]

[a] Department of Materials Science and Engineering and State Key Lab for Materials Processing and Die & Mould Technology, Huazhong University of Science and Technology, Wuhan 430074, People's Republic of China

[b] State Key Laboratory of Nonlinear Mechanics, Institute of Mechanics, Chinese Academy of Sciences, Beijing 100190, People's Republic of China

[c] Department of Physics and Astronomy, University of North Carolina at Chapel Hill, Chapel Hill, NC 27599-3255, USA

Received 7 November 2012; received in revised form 5 December 2012; accepted 11 December 2012
Available online 10 January 2013

Abstract

A thermoplastic forming (TPF) map of a $Zr_{35}Ti_{30}Be_{26.75}Cu_{8.25}$ bulk metallic glass was constructed through systematic hot-embossing experiments, spanning a wide range of strain rates and temperatures in the supercooled liquid region. By comparison with the corresponding deformation map, it is found that Newtonian flow, non-Newtonian flow and inhomogeneous flow regions correspond well to fully filled, partially filled and non-filled regions, respectively, in the hot-embossing TPF map. Furthermore, the spatio-temporally homogeneous flow facilitates the thermoplastic formabillity of the Zr-based bulk metallic glass, which is rationalized in terms of free volume theory as well as by finite element simulations. Finally, our results are corroborated by potential application tests.

Keywords: Metallic glass; Thermoplastic forming map; Deformation map; Free volume; Formability

1. Introduction

Bulk metallic glasses (BMGs) exhibit different flow features compared to their crystalline counterparts, due to the absence of long-range order and dislocation-like defects [1–7]. Dependent on temperature, stress and strain (rate), the flow of BMGs can be homogeneous or inhomogeneous not only spatially but also temporally, which is usually characterized by a deformation or flow map (a convenient means of surveying the various modes of plastic deformation of a material) [4,8]. Based on systematical examination of the deformation and fracture in metallic glasses, Spaepen [8] first constructed a deformation map that distinguishes the plastic deformation into two basic modes: homogeneous and inhomogeneous. For the former, each volume element of the sample contributes to the macroscopic plastic strain [8]; for the latter, the strain is highly localized into a few nanoscale shear bands [9–13]. The deformation map has been subsequently extended by a number of other researchers [4,14–17]. For example, Schuh et al. [16] discovered a new regime of homogeneous flow ("Homogeneous II") that lies at the top right corner of the original deformation map of Spaepen [8]. Furthermore, Schuh et al. [4] reconstructed the deformation map that differentiates "Newtonian" and "non-Newtonian" flow in the homogeneous regime. The underlying physical mechanism for the deformation map of metallic glasses has been explained well by a shear-transformation-zone or free-volume-mediated flow mechanism [4,8,14,17].

Taking advantage of BMGs' superplastic flow in the supercooled liquid region (SCLR), thermoplastic forming (TPF) has been widely employed to fabricate precise and versatile geometries on length scales ranging from 10 nm to several centimeters [18–36]. The formability has been proposed to be the key property that determines the suitability of BMGs for TPF [37–42]. For metallic glasses of different alloy systems, the smallest replicated features [5,31,43], the maximum plastic strain that related to the large Poisson ratio and low glass transition [41] and other parameters, such as fragility and thermal stability [37,38,44–47], have been discovered to be associated with

* Corresponding author. Tel.: +86 27 87556894; fax: +86 27 87554405.
E-mail address: lliu2000@mail.hust.edu.cn (L. Liu).

1359-6454/$36.00
http://dx.doi.org/10.1016/j.actamat.2012.12.013

BMGs' formability. However, for a metallic glass with a certain composition, the temperature-dependent viscosity and long processing time [5,28,42] are regarded as the two parameters that can most significantly affect the formability of BMGs. That increasing temperature favors formability can be understood well from the viewpoint of lowering viscosity. Whereas the decrease in viscosity with increasing strain rate at a certain temperature inherently induces a transition from Newtonian to non-Newtonian flow, this makes TPF much more difficult, and causes contradictory results. For instance, this transition was found to result in a dramatic decrease in tensile extensibility in a Pd-based BMG [48]. In particular, it was reported that Newtonian flow corresponding to significant structural rearrangement during TPF assists viscous flow with less thermal dissipation, and enhances the high-temperature formability of BMGs [49–52]. Accordingly, the exact relationship between the formability and the flow characteristic of BMGs during TPF is still unclear [4,48–50,53]. One main reason for this is that no TPF map of a BMG has been constructed experimentally yet, unlike deformation maps. In the present work, we develop a TPF map for a Zr-based BMG based on a series of hot-embossing experiments at various strain rates and temperatures in the SCLR. This hot-embossed TPF map allows us to make a comprehensive comparison with the deformation map obtained from the corresponding uniaxial compression experiments under the same conditions. The underlying mechanism is analyzed from the viewpoint of spatio-temporally homogeneous/inhomogeneous flow based on free volume theory and finite element method simulation. Finally, potential application tests are carried out to validate the present results.

2. Experimental

A $Zr_{35}Ti_{30}Be_{26.75}Cu_{8.25}$ BMG system was chosen for this study because of its excellent anti-oxidation capability, large supercooled liquid region, good glass forming ability and high fragility [54]. Rods of this BMG, with a diameter of 6 mm and a length of 60 mm, were fabricated by arc-melting a mixture of pure Zr, Ti, Be and Cu metals (purity > 99.5%) under a Ti-gettered argon atmosphere, followed by suck casting into copper molds. The glassy structure of the as-cast alloy was verified by X-ray diffraction (Philips χ' Pert Pro) and transmission electron microscopy (Jeol-2010). The thermal response was determined by differential scanning calorimetry (DSC; Perkin–Elmer DSC-7) at a heating rate of 20 K min^{-1}, showing a glass transition temperature (T_g) of 307 °C with a supercooled liquid region of 141 °C. The isothermal crystallization experiments were carried out by DSC at various temperatures, which revealed that the incubation time is around 1 min at 450 °C, 10 min at 410 °C, 150 min at 390 °C and more than 300 min at 370 °C. The results are identical to the time–temperature–transformation diagrams measured by Duan et al. [54]. The whole duration of the hot-embossing process at various temperatures and strain rates was carefully controlled within the incubation time of the BMG to avoid any possible crystallization. BMG samples with a height of 1.5 mm and a diameter of 6 mm for hot-embossing experiments were obtained by wire-cutting from the as-cast amorphous rods.

A microchannel which is 50 μm wide, 100 μm deep and 200 μm spacing, was used for TPF. The channel involves straight portions, single and continuous bends [36]. The designed three-dimensional (3-D) profile is described in Fig. 1a. Fig. 1b shows the steps of silicon master mold fabrication, the details of which have been described elsewhere [31]. The independent silicon master mold used for hot-embossing, with a square of 4.5 mm × 4.5 mm, was cut from a 4 in. diameter silicon wafer.

A schematic of the hot-embossing process is presented in Fig. 1c, and is similar to what was reported previously [19,31,32,39]. Hot-embossing experiments were performed at various temperatures, ranging from 310 to 390 °C, in the SCLR, with strain rates ranging from 5×10^{-4} to 1×10^{-1} s^{-1}, using a Zwick machine (Zwick/Roell 020) equipped with an air furnace. In this temperature regime, the incubation time for crystallization is longer than 150 min, which provides a sufficient time window for sample handing and hot-embossing without the risk of crystallization. In order to shorten the time for heating the sample, the load train was preheated to the test temperature and held for 30 min to stabilize the temperature, the BMG specimen was stacked onto silicon master mold and then rapidly placed into the load train with a preload of about 0.5 MPa and held for another 2 min to attain thermal equilibrium. The fluctuation of temperature in the furnace during testing was about ±1 K. After the hot-embossing process, the embossed metallic glass part was separated from the silicon mold by etching away the silicon in a KOH bath, as shown in Fig. 1d. Micrographs of the hot-embossed Zr-based BMG with microchannel structures were observed by scanning electron microscopy (SEM; Qutanta 400), and the filling depths (h) were measured according to the side morphologies.

3. Results

Fig. 2a illustrates a typical microchannel pattern hot-embossed on the Zr-based BMG surface at a temperature of 370 °C and a strain rate of 1×10^{-3} s^{-1}. It can be clearly seen that the hot-embossed microchannel is printed well, with no obvious disfigurement, displaying a good geometrical transferability in the selected experimental condition. To reveal the uniformity of the filling depth, the side view is presented in Fig. 2b and c. The top surfaces of the hot-embossed channel are parallel and level to each other, indicating that the channel is fully filled.

To examine the effect of temperature on the formability of the BMG, the hot-embossing was conducted at various temperatures. Fig. 3 shows the morphology and side views of the continuous bends at a certain strain rate of

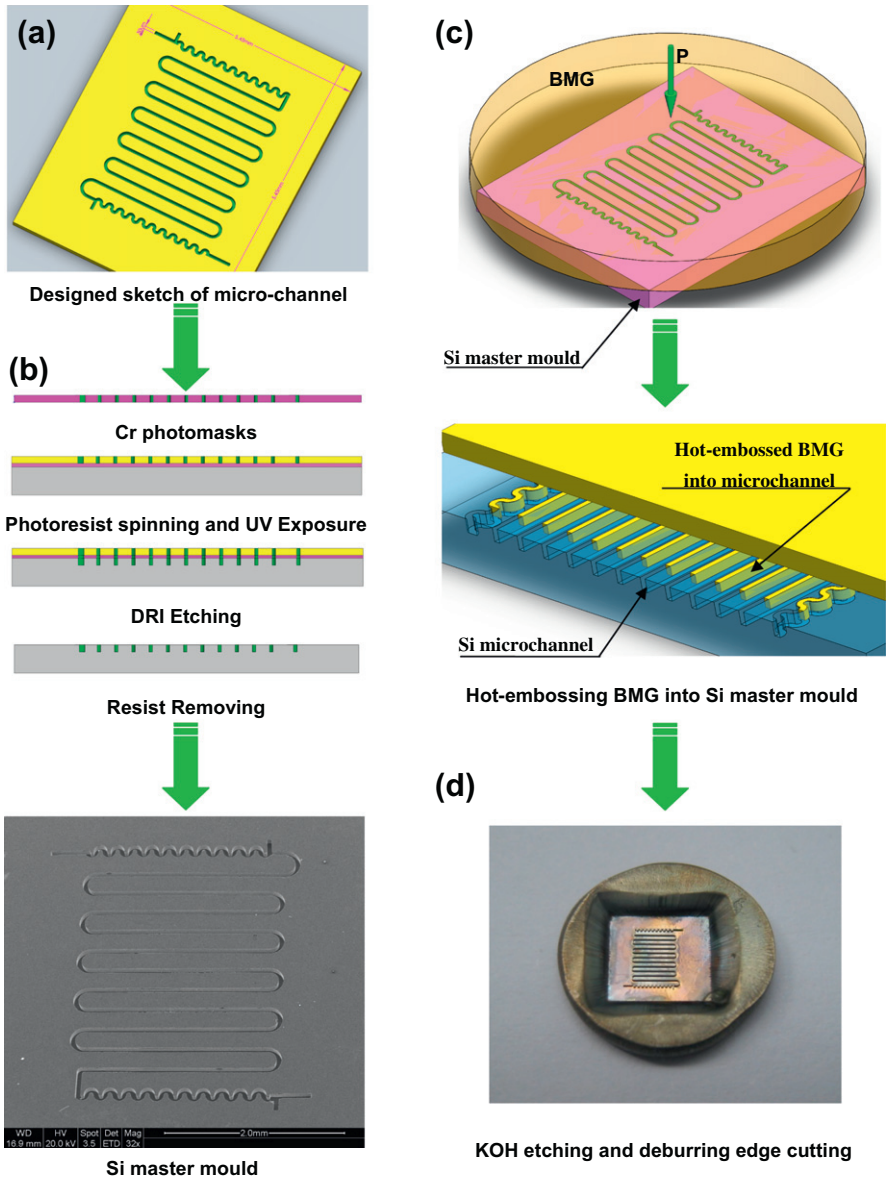

Fig. 1. Schematics of the hot-embossing process. (a) 3-D sketch of the designed microchannel patterns. (b) The manufacturing steps of the silicon master mold, including photomask writing, photoresist spinning and UV exposure, deep reactive ion etching of the exposed regions, residual photoresist removal and silicon master mold characterization. (c) The Zr-based BMG is hot-embossed into the silicon master mold. (d) Zr-based BMG microchannel structure is released by etching the Si wafer in KOH.

$1 \times 10^{-3}\ s^{-1}$ and at temperatures from 310 to 390 °C. At the low temperature of 310 °C, the hot-embossed surface is flat without any patterns, as described in Fig. 3a and b, indicating that the Zr-based metallic glass was hardly hot-embossed at this low temperature. When the temperature increases to 330 °C, the sketch of the channel appears (see Fig. 3c). The corresponding filling depth h is about 5.83 μm, as measured from the side morphology (see Fig. 3d). This tendency becomes more prominent at higher temperatures, such as at 350 °C, when the value of the channel's height sharply increases up to about 62.5 μm (see Fig. 3e and f). The microchannel pattern in silicon master was fully filled by the Zr-based metallic glass at 390 °C (see Fig. 3g and h), as the height of the channel reaches the depth of the silicon mold (~100 μm).

The effect of the strain rate on the formability of the BMG was also investigated. Fig. 4 shows the morphology and side view of the continuous bends of the channel at the single temperature of 370 °C, but at different strain rates, ranging from 1×10^{-3} to $1 \times 10^{-1}\ s^{-1}$. Complete filling was realized at the relatively low strain rates of 1×10^{-3} and $5 \times 10^{-3}\ s^{-1}$, in which the filling depth reaches about 100 μm, as shown in Fig. 4a–d, respectively. However, partial filling occurs at higher strain rates; for example, at a strain rate of $1 \times 10^{-2}\ s^{-1}$, the corresponding filling depth decreases to 38.5 μm (see Fig. 4e and f). When the strain rate increases up to $1 \times 10^{-1}\ s^{-1}$, the hot-embossed channel's depth is only about 7.75 μm (see Fig. 4g and h), highlighting the very limited formability of the Zr-based BMG at high strain rate.

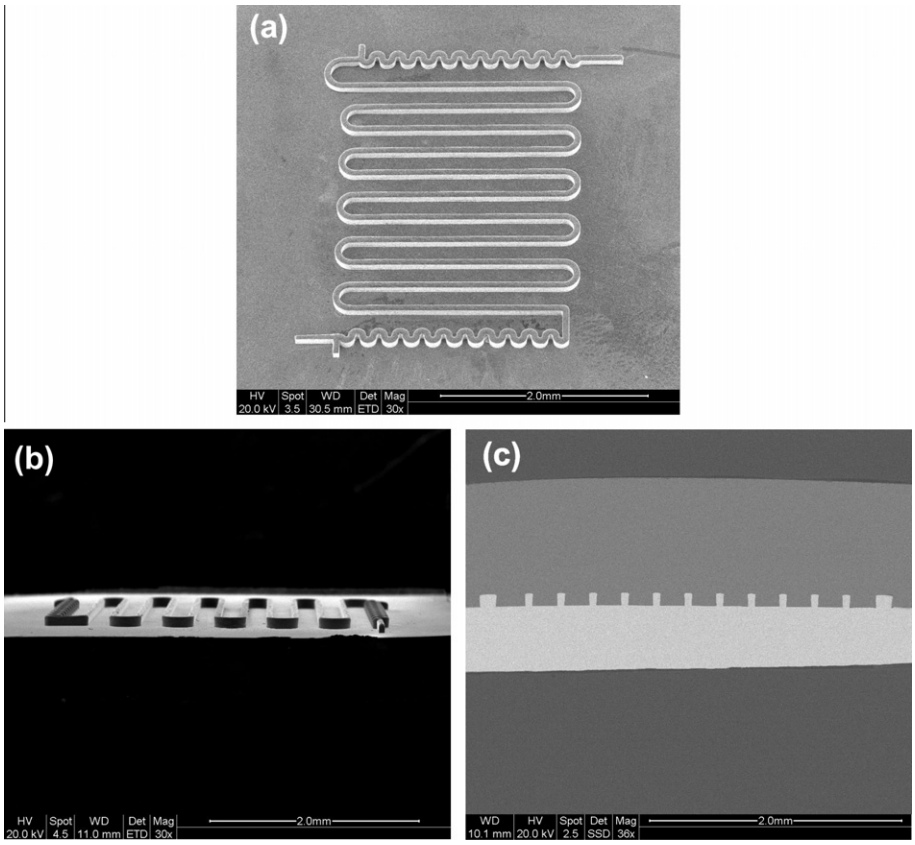

Fig. 2. SEM micrographs of the hot-embossed microchannel pattern at a temperature of 370 °C and a strain rate of $1 \times 10^{-3}\ s^{-1}$ (a), and the corresponding side (b) and cross-section (c) morphologies.

The filling depths at various temperatures and strain rates are summarized in Fig. 5. The maximum value of h, i.e. 100 μm, indicating complete filling, can be observed at the high temperatures of 370 and 390 °C across a large range of strain rates, i.e. $\dot{\varepsilon} \leqslant 5 \times 10^{-3}\ s^{-1}$ for 370 °C and $\dot{\varepsilon} \leqslant 1 \times 10^{-2}\ s^{-1}$ for 390 °C. Beyond these strain rates, the value of h reduces rapidly with increasing strain rate. This phenomenon is also observed at low temperatures, from 310 to 350 °C. At a certain strain rate, on the other hand, the value of h reduces with decreasing temperature, and even drops to nearly zero at a temperature below 350 °C, showing strong temperature dependence.

According to the systematic experimental results, we can construct a TPF map that describes the correlation of formability characterized by the filling height with the strain rate and temperature, as shown in Fig. 6. Here, the processing temperature is normalized by the glass transition temperature (T_g). Three distinct regimes can be observed in Fig. 6: a fully filled regime in the bottom right-hand corner (corresponding to low strain rates or/and high temperatures), a non-filled regime in the top left-hand corner (corresponding to high strain rates or/and low temperatures) and a partially filled regime in between. This forming map can be compared to the deformation maps at various strain rates and temperatures in previous works [4,49–51,53], implying that there exists a close correlation between formability and deformation behavior.

The deformation map in the stress-and-strain-rate space is shown in Fig. 7 based on a series of uniaxial compression tests under the same conditions as used in the hot-embossing experiments (Supplementary material). According to the value of the strain rate sensitivity (m), the deformation map can be divided into three regions: a Newtonian homogeneous flow region, a non-Newtonian homogeneous flow region and an inhomogeneous flow region. Interestingly, these three regions fit well with the fully filled, partially filled and non-filled regimes in the TPF map, respectively. It is widely accepted that Newtonian homogeneous flow means that the flow is homogeneous not only temporally but also spatially. The consistency between the TPF map and the deformation map indicates that the Newtonian homogeneous flow favors TPF of the BMG in the SCLR.

4. Discussion

4.1. Theoretical analysis based on free volume theory

During the TPF process, the high viscosity of BMG supercooled liquid implies that the Reynolds number value is within the creeping flow regime [55]. Thus, in the hot-embossing process, the flow of the BMG in a channel

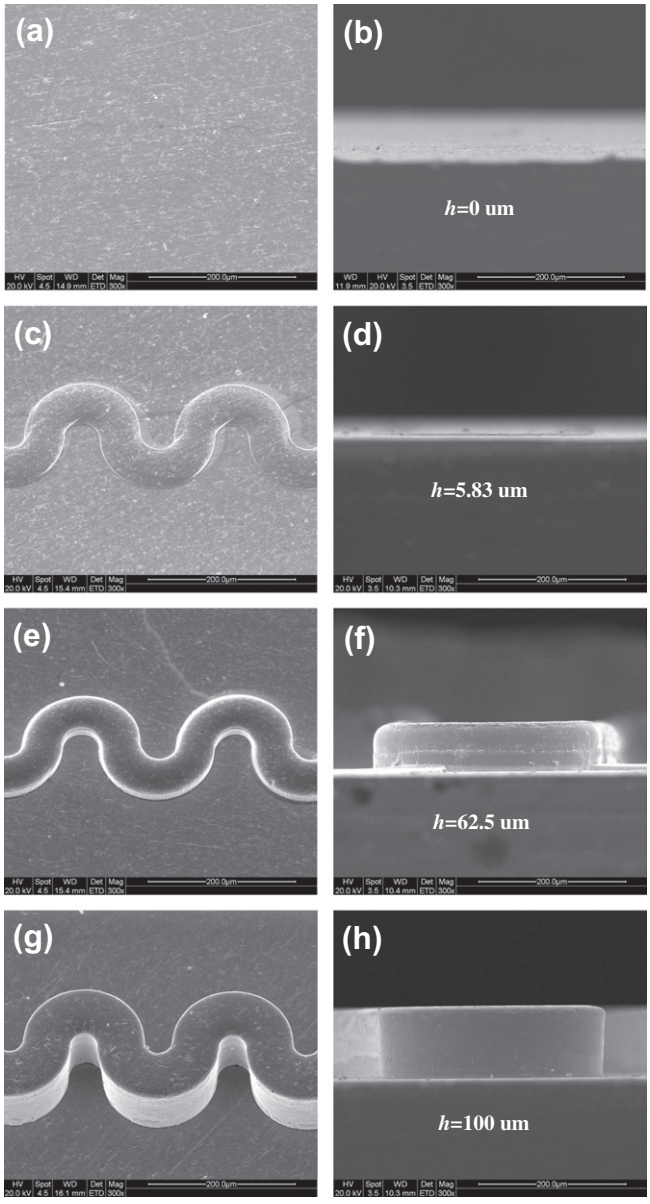

Fig. 3. SEM micrographs of the hot-embossed microchannel pattern with continuous bends and side views at temperatures of 310 °C (a and b), 330 °C (c and d), 350 °C (e and f) and 390 °C (g and h) under a strain rate of $1 \times 10^{-3}\ s^{-1}$.

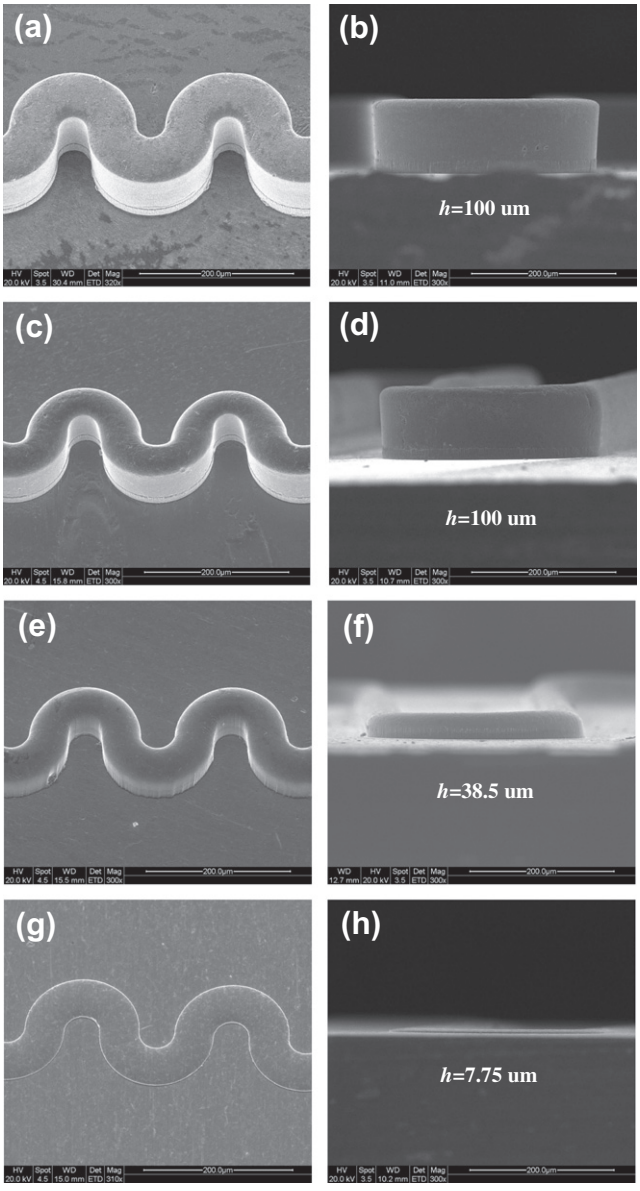

Fig. 4. SEM micrographs of the hot-embossed microchannel pattern with continuous bends and side views at strain rates of $1 \times 10^{-3}\ s^{-1}$ (a and b), $5 \times 10^{-3}\ s^{-1}$ (c and d), $1 \times 10^{-2}\ s^{-1}$ (e and f) and $1 \times 10^{-1}\ s^{-1}$ (g and h) at a temperature of 370 °C.

with a width of d and a length of h can be considered as a laminar flow that obeys the Hagen–Poiseuille law [28,31]

$$p = \frac{16V\eta(\dot{\varepsilon}, T)}{d^2}h \tag{1}$$

where p is the required pressure to move the BMG liquid with the viscosity of $\eta(\dot{\varepsilon}, T)$ (as a function of the strain rate $\dot{\varepsilon}$ and temperature T) into a channel with a width of d and depth of h. Approximating the filling velocity V to be $h\dot{\varepsilon}$, then Eq. (1) can rewritten as

$$h = \sqrt{\frac{pd^2}{16\eta(\dot{\varepsilon}, T)\dot{\varepsilon}}} \tag{2}$$

The experimental results indicate that the filling depth approaches zero at low temperature near T_g (see Figs. 3a and b and 5). Hence, a fictive filling depth h_f at T_g is assumed to normalize the calculation, and then the theoretical filling depth (h_t) during hot-embossing can be formulated as

$$h_t = \sqrt{\frac{pd^2}{16\eta(\dot{\varepsilon}, T)\dot{\varepsilon}}} - h_f \tag{3}$$

where $h_f = \sqrt{\frac{p_{Tg}d^2}{16\eta(\dot{\varepsilon}, T_g)\dot{\varepsilon}}}$ with a forming pressure (p_{Tg}) of 100 MPa at $T_g = 307$ °C according to the uniaxial compression results (Supplementary material). It should be

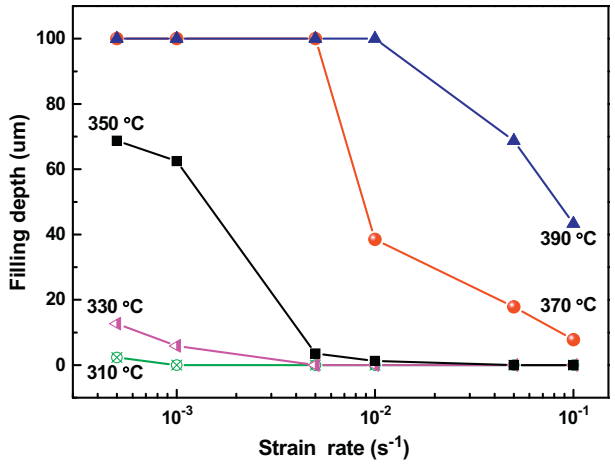

Fig. 5. The hot-embossing filling depths at various temperatures and strain rates.

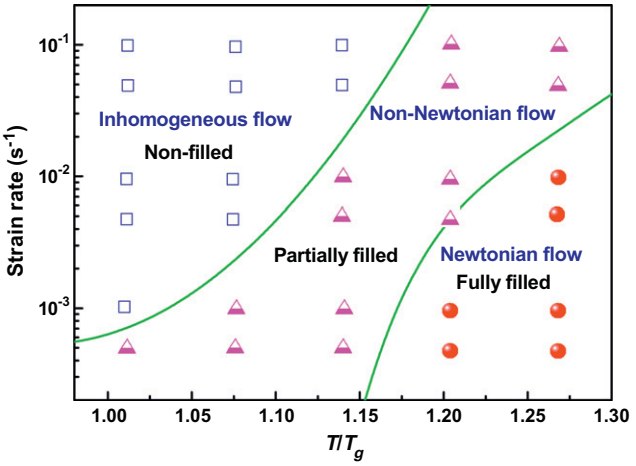

Fig. 6. Thermoplastic forming map with three fundamental elements, namely non-filled, partially filled and fully filled regimes.

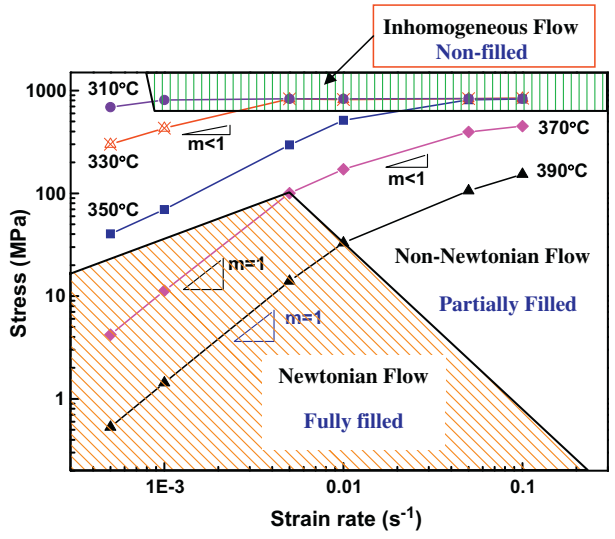

Fig. 7. A deformation map for the Zr-based BMG obtained by compression tests (Supplementary material), describing the transition from Newtonian flow to non-Newtonian flow.

noted that the viscosity η is proposed to be the main parameter controlling the formability of BMGs and is reflected by the fragility of various BMG alloy systems [28,41,42]. However, for a BMG with a certain composition, viscosity shows sensitivity to both temperature and strain rate. These temperature and strain rate parameters usually induce a transition from Newtonian to non-Newtonian flow within the homogeneous regime in SCLR, and affect the formability of BMGs [4,48]. These characteristics can be captured well by a phenomenological viscosity law proposed by Johnson et al. [56] based on the free volume model of Cohen and Grest (the CG model) [57], in which the viscosity of the BMG in the TPF process is illustrated by [56]

$$\eta(\dot{\varepsilon}, T) = \frac{\eta_0}{D(\dot{\varepsilon}, T)} \exp\left(\frac{\alpha}{\upsilon_T}\right) \tag{4}$$

where $\upsilon_T = \frac{1}{2d_1}\left[T - T_{ref} + \sqrt{(T - T_{ref})^2 + d_2 T}\right]$ is the temperature-dependent free volume concentration (FVC) in the CG model. d_1, d_2 and T_{ref} are material parameters; for amorphous $Zr_{41.2}Ti_{13.8}Cu_{12.5}Ni_{10}Be_{22.5}$ (Vit1), $d_1 = 46981$ K, $T_{ref} = 672$ K and $d_2 = 183$ K [58]. This CG relation is defined well when the temperature is lower than T_{ref} and approaches the Vogel–Rulcher–Tammann relation at high temperature. Parameter $D(\dot{\varepsilon}, T) = 1 + \exp\left(\frac{\alpha}{\upsilon_T}\right)\left(\frac{\eta_0 \dot{\varepsilon}}{\sigma_0}\right)^{b(T)}$. Here, α is a geometrical factor of order unity, η_0 is the viscosity of the liquid at the high-temperature limit, σ_0 is a reference stress, and the temperature-dependent $b(T)$ is a stretching exponent fitting from the data [56]. For Vit1 BMG [59], $\alpha = 0.105$, $\eta_0 = 4 \times 10^{-5}$ Pa s, $\sigma_0 = 0.25\sigma_y$, σ_y is the yield stress at room temperature ($\sim$1.9 GPa) and $b(T) = 1.0 - \alpha_\eta(T - T_\eta)^3$, with $\alpha_\eta = 4.325 \times 10^{-10}$ K^{-3} and $T_\eta = 293$ K. Considering that the BMG used in the present work has a similar composition to Vit 1, the above parameters can be used in the current calculations.

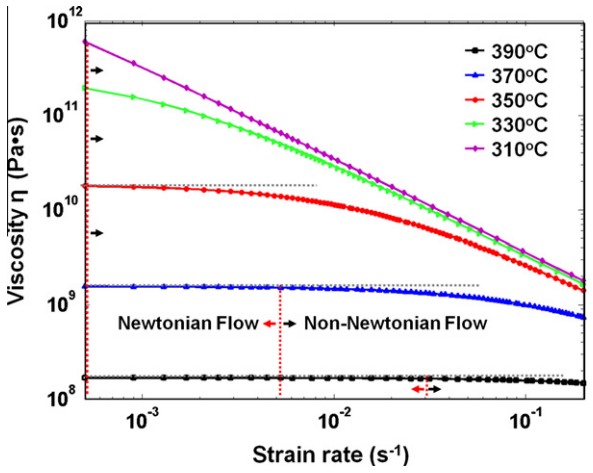

Fig. 8. The calculated viscosity of the Zr-based BMG changes with strain rates and temperatures.

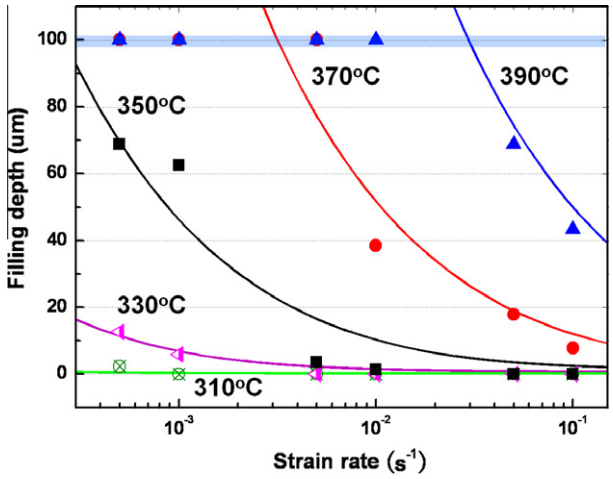

Fig. 9. Calculated (curves) and experimental (datum points) filling depths at various strain rates and temperatures.

According to Eq. (4), a viscosity dependence on strain rate and temperature is constructed and depicted in Fig. 8. Similar to what was observed in previous work [56,60], the calculated viscosity shows a strong strain rate dependence at low temperatures. For instance, at a temperature below 350 °C, the viscosity decreases monotonously with increasing strain rate, indicating a non-Newtonian behavior. However, when the temperature reaches 370 °C and above, the viscosity remains constant within a certain range of strain rate ($\leqslant 5 \times 10^{-3}\,s^{-1}$), then decreases with further increasing strain rate. This critical strain rate for the Newtonian to non-Newtonian transition increases up to $1 \times 10^{-2}\,s^{-1}$ at the higher temperature of 390 °C, in accordance with what was observed in experiments (see Fig. 5).

Using the data of viscosity in Fig. 8, Eq. (3) yield plots of filling depth (h) vs. strain rate ($\dot{\varepsilon}$) at various temperatures, as depicted in Fig. 9. It is interesting to find that the $h-\dot{\varepsilon}$ curves show a quite similar tendency to the experimental results at various temperatures and strain rates. For example, the maximum filling depths of both experiment and calculation are around 100 μm while, for a filling depth below 100 μm, the experimental data also fit the calculated curves well, showing good consistency.

Comparing Figs. 8 and 9, one can see that the transition from full filling to partially filling shown in Fig. 9 corresponds to the transition from Newtonian to non-Newtonian flow. This transition reflects the strain rate sensitivity, which is related to the temporal inhomogeneity in atomic scale flow. Therefore, the correlation between TPF formability and temporal homogeneity can be revealed from the free volume point of view. Considering the effect of strain rate on free volume evolution and assuming $\eta(\dot{\varepsilon},T)=\eta_0\exp\left(\frac{\alpha}{\upsilon(\dot{\varepsilon},T)}\right)$ is satisfied for both Newtonian and non-Newtonian flow regimes, then the FVC $\upsilon(\dot{\varepsilon},T)$ can be derived from Eq. (4), and is expressed as

$$\upsilon(\dot{\varepsilon},T)=\frac{1}{1/\upsilon_T-\ln D(\dot{\varepsilon},T)/\alpha} \tag{5}$$

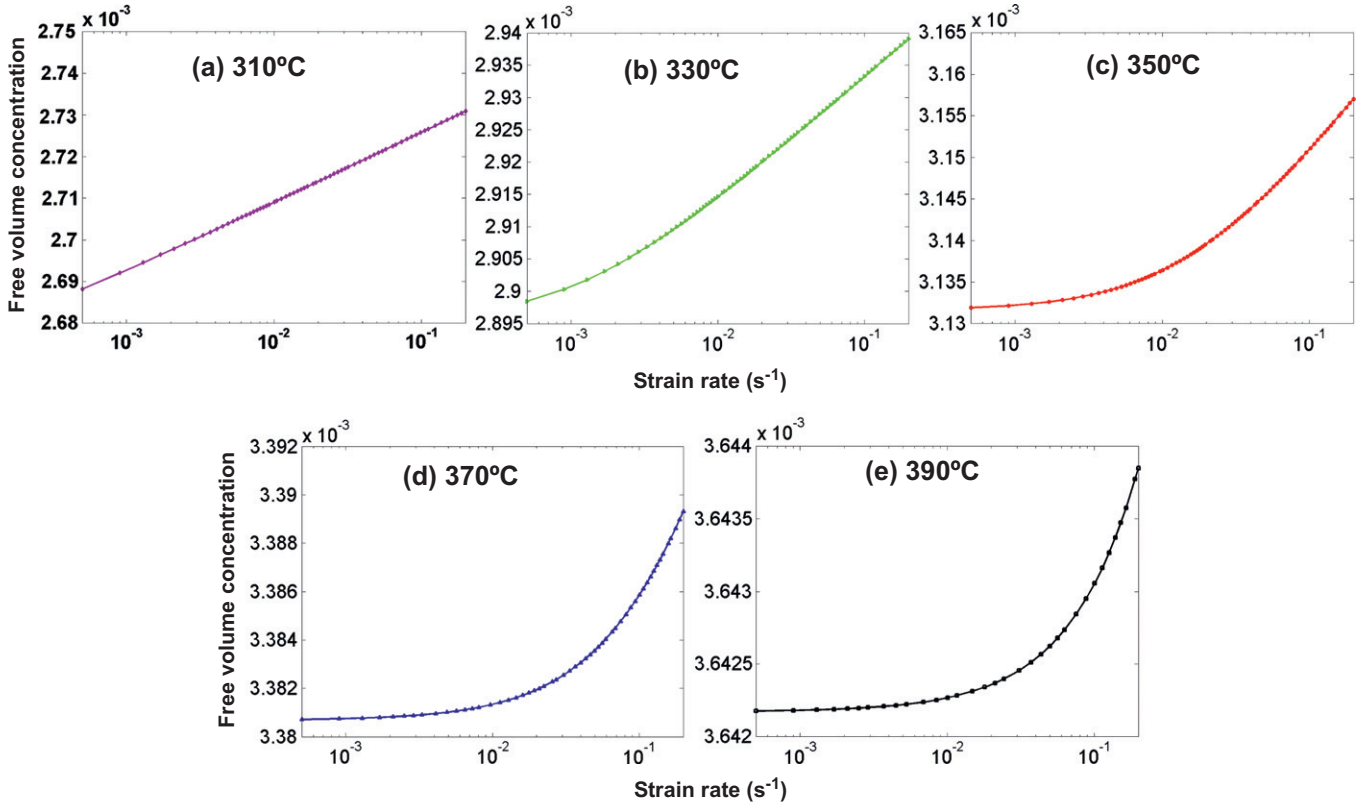

Fig. 10. Evolution of free volume concentration with strain rates at different temperatures.

Based on Eq. (5), the plots of FVC at various temperatures and strain rates are obtained, as delineated in Fig. 10. It can be seen that the FVC of the BMG liquid increases with increasing temperature at a fixed strain rate, showing temperature dependence [61]. In addition, the FVC also shows strain rate dependence; for example, the FVC increases monotonously with increasing strain rate when the temperature is below 350 °C across a wide range of strain rates ($\geqslant 5 \times 10^{-4} s^{-1}$) (see Fig. 10a–c). In this case, FVC displays an unsteady change with time, resulting in a change in viscosity (see Fig. 8). Therefore, there are heterogeneities for the viscosity and FVC in the BMG liquid during plastic forming, resulting in an unsteady flow. The regions with low viscosity (or high FVC) could flow fast,

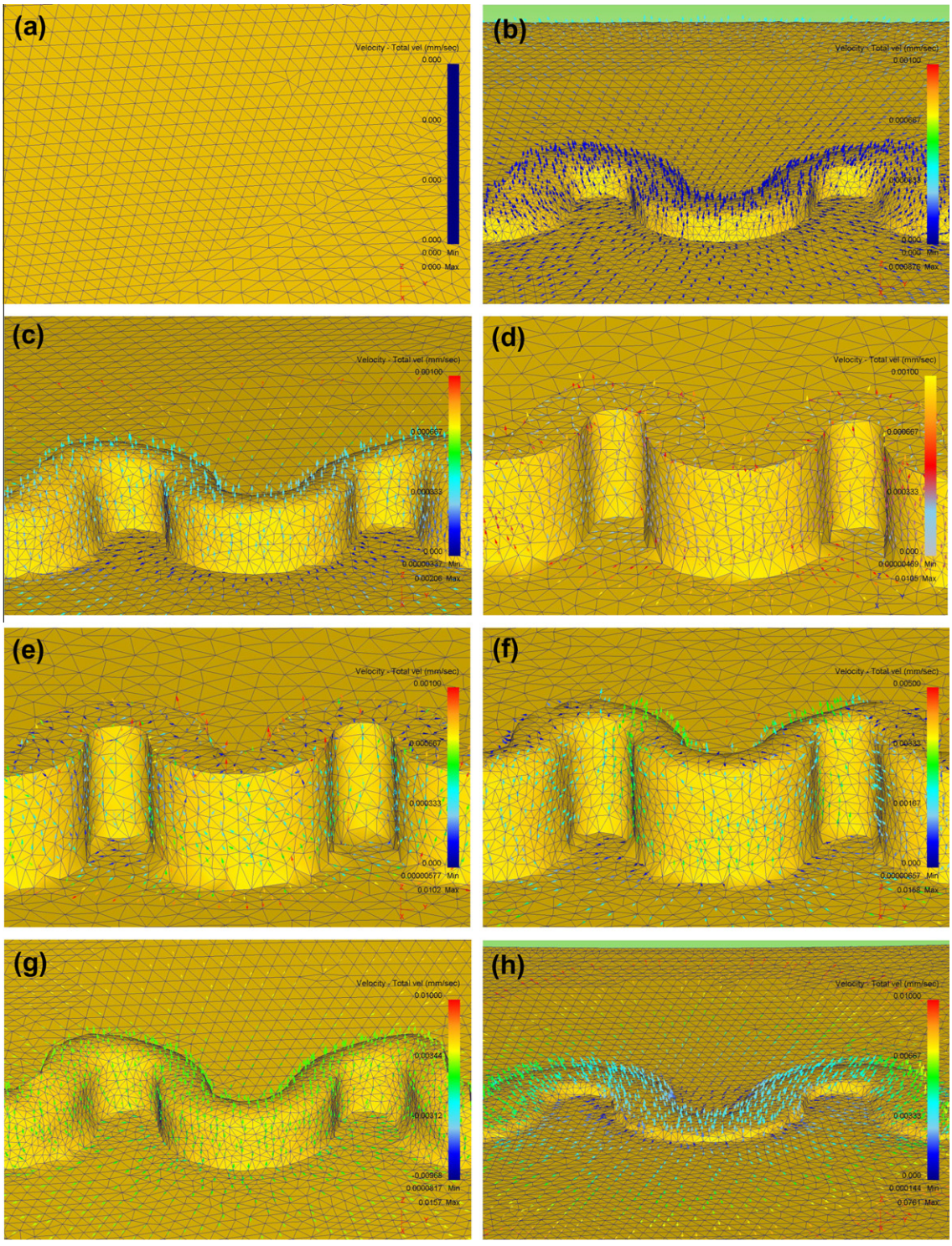

Fig. 11. 3-D continuous bends simulated at various temperatures: (a) 310 °C, (b) 330 °C, (c) 350 °C, (d) 390 °C at strain rate of $1 \times 10^{-3}\ s^{-1}$; and at different strain rates: (e) $1 \times 10^{-3}\ s^{-1}$, (f) $5 \times 10^{-3}\ s^{-1}$, (g) $1 \times 10^{-2}\ s^{-1}$, (h) $1 \times 10^{-1}\ s^{-1}$ at a temperature of 370 °C.

but these regions can be restrained by the regions with high viscosity (or low FVC). The interactions between different regions with different viscosities (different FVCs) can slow down the whole flow velocity and thus degrade the formability. On the other hand, at high temperatures (above 350 °C), a flat line before rising can be observed at a certain range of strain rates, $\sim 10^{-3}\ s^{-1}$ at 370 °C and $\sim 10^{-2}\ s^{-1}$ at 390 °C, indicating achievement of a balance between creation and annihilation of free volume at high temperature. This favors continuous and steady operation of plastic units (i.e. shear transformation zones), and facilitates the formability. The similar effect of temperature on formability was also found in previous work [48–51,53]. However, when the strain rate keeps increasing, the strain rate sensitivity of FVC appears again, resulting in a transition from temporal homogeneity to inhomogeneity.

4.2. Finite-element simulations

To further examine the spatial homogeneity and inhomogeneity of the Zr-based BMGs during hot-embossing, we resort to the commercial software DEFORM 2D and 3D in this section. Since the channels are long enough compared to their width, and there are a large number of them aligned in parallel, we employed a plane strain idealization in our simulations and consider only continuous bends with suitable boundary conditions [26,36]. A friction coefficient of 0.25 between the silicon and the metallic glass was selected. A Maxwell constitutive model that we proposed [62] is defined using the data from our uniaxial compressive test at various temperatures and strain rates.

Fig. 11 shows the 3-D profile of the velocity distributions simulated under the same conditions as those used in the experiments. From Fig. 11a, a flat surface without any profile of the channel can be observed, indicating a non-filled regime at the low temperature of 310 °C. At higher temperatures, such as 330 °C (see Fig. 11b) and 350 °C (see Fig. 11c), the Zr-based BMG was hot-embossed into the microchannel and the filling depth increased with increasing temperature, showing a partial filling regime. At the highest temperature of 390 °C (see Fig. 11d), the metallic glass at the top portion moves towards the verge of the channel with nearly zero velocity, indicating that the metallic glass has holistically touched the bottom of the silicon mold. The simulated velocity distributions, on the other hand, also reflect strain rate dependence, as described in Fig. 11e–h. The microchannel was fully filled at a strain rate of $1 \times 10^{-3}\ s^{-1}$ (see Fig. 11e). However, at the higher strain rate of $5 \times 10^{-3}\ s^{-1}$ (see Fig. 11f), a curved surface can be observed at the top section, and the filling depth decreases continuously with increasing strain rate (see Fig. 11g and h). Therefore, the

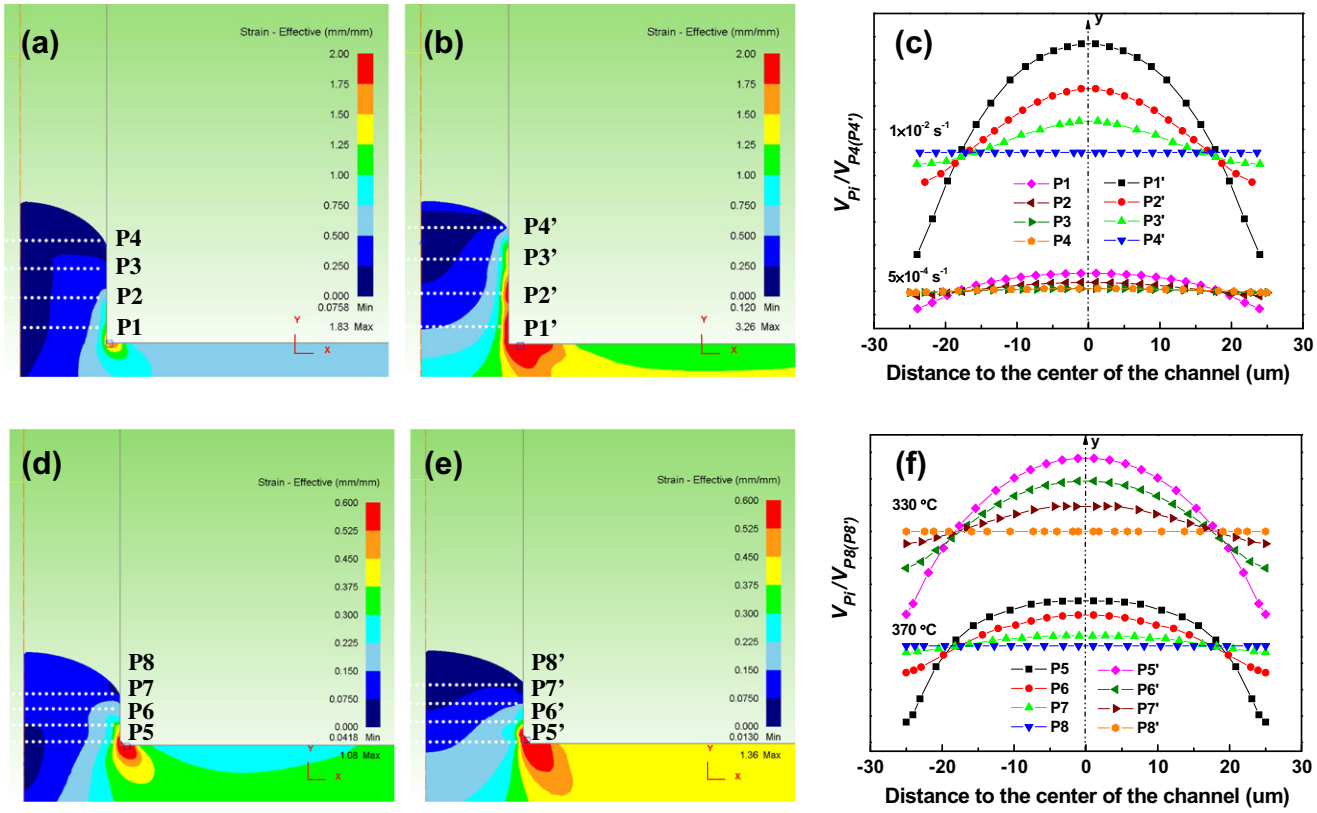

Fig. 12. The simulated effective stain distribution during hot-embossing at a fixed temperature of 370 °C with strain rates of $5 \times 10^{-4}\ s^{-1}$ (a) and $1 \times 10^{-2}\ s^{-1}$ (b); and at a fixed strain rate of $5 \times 10^{-4}\ s^{-1}$ with temperatures of 370 °C (d) and 330 °C (e). (c) and (f) show the corresponding speed distribution at different positions.

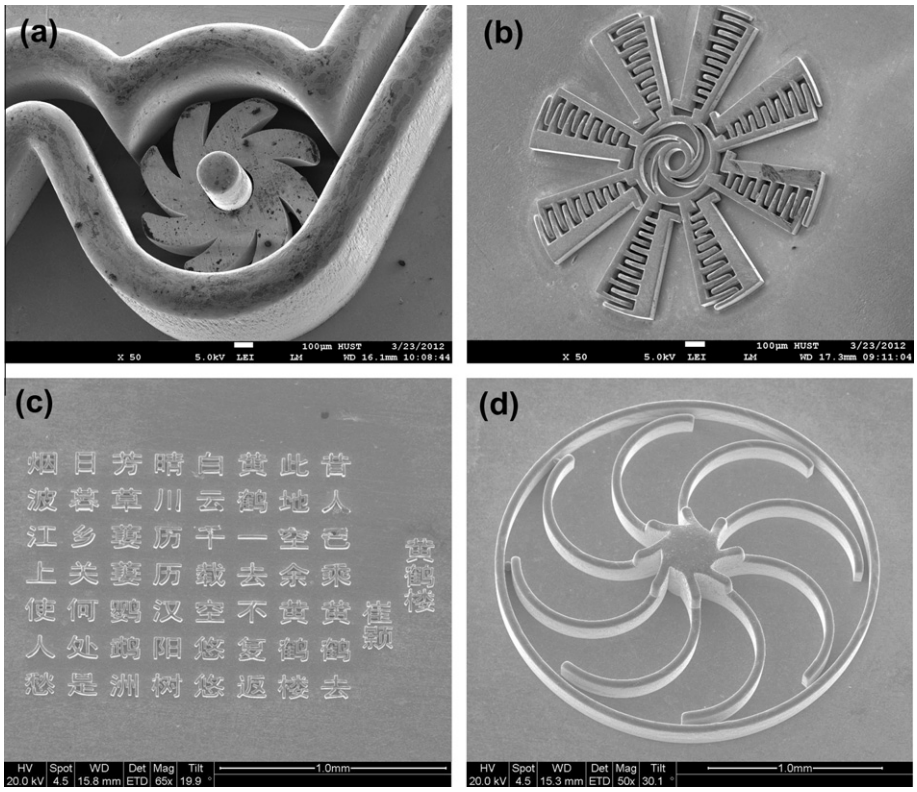

Fig. 13. SEM microscopy of the micropump used in a cardiac pacemaker (a), a microgyroscope (b), the famous Tang Dynasty poem "Yellow Crane Tower" (c) and a corrugated microfan (d), hot-embossed in a Newtonian flow region (i.e. a temperature of 370 °C and a strain rate of $1 \times 10^{-3}\ s^{-1}$).

simulated results in Fig. 11 are consistent with what was observed in the corresponding experiments (Figs. 3 and 4), demonstrating the validity of our simulations.

Fig. 12a and b illustrates the distribution of plastic strain simulated at 5×10^{-4} and $1 \times 10^{-2}\ s^{-1}$, respectively, under the temperature of 370 °C. As expected, the plastic strain is greatest at the corner of the channel, indicating local heterogeneous distribution of the strain. It is worth pointing out that, on the whole, the distribution of plastic strain is relatively homogeneous at the strain rate of $5 \times 10^{-4}\ s^{-1}$ (see Fig. 12a), unlike what was observed at the higher strain rate of $1 \times 10^{-2}\ s^{-1}$ (see Fig. 12b). The corresponding velocity fields at positions P1 (P1′)–P4 (P4′) under the two strain rates are shown in Fig. 12c, where the minimum velocity at P4 (P4′) is taken as a reference. It is obvious that all curves show a higher velocity value at the center of the channel, while the flow speed decreases towards to the interface between the metallic glass and the master silicon mold, exhibiting a velocity gradient. To clearly distinguish the differences in the velocity gradient at various strain rates, all of the curves obtained at $5 \times 10^{-4}\ s^{-1}$ were shifted along the speed axis by a value of 0.3. However, the difference in the velocity gradient from P1–P4 for the BMG hot-embossed at strain rate of $5 \times 10^{-4}\ s^{-1}$ is less than that of $1 \times 10^{-2}\ s^{-1}$, showing a more uniform flowing during TPF at a low strain rate, which facilitates the formability and finally increases the filling depth. The distribution of equivalent plastic strain at temperatures of 370 and 330 °C under a certain strain rate of $1 \times 10^{-3}\ s^{-1}$ was also simulated, as depicted in Fig. 12d and e, respectively. The distribution of flow speeds at locations P5 (P5′)–P8 (P8′) is shown in Fig. 12f. Similar to the effect of strain rate, the increase in TPF temperature brings a more uniform flow reflected by equivalent plastic strain and speed fields. Our simulated results further confirm that the spatially homogeneous flow favors the hot-embossing formability.

To confirm that Newtonian flow can favor the formability of the BMG, a few patterns and microparts which are useful in microelectromechanical systems were hot-embossed at 370 °C and at a strain rate of $1 \times 10^{-3}\ s^{-1}$ (the temperature and strain rate fall in the Newtonian flow region, as described in the deformation map), and are shown in Fig. 13. It can be seen clearly that the embossed structures are integrated without any obvious disfigurement, especially for the famous Chinese poem "Yellow Crane Tower" [63], for which the line width is less than 5 μm. The results demonstrate that the Newtonian homogeneous flow facilitates the TPF formability, which is important for the TPF of BMGs.

5. Conclusions

We have performed a series of hot-embossing experiments for $Zr_{35}Ti_{30}Be_{26.75}Cu_{8.25}$ bulk metallic glass on a silicon wafer with microchannel patterns at various strain

rates and temperatures in the supercooled liquid region. The results revealed an inherent relationship between the thermoplastic formability and the flow characteristics, i.e. Newtonian flow, facilitates the forming capability, while TPF in a non-Newtonian flow regime tends to be difficult. It is suggested that such an agreement between the TPF map and deformation map corresponds to the spatio-temporally homogeneous/inhomogeneous flow of metallic glass during hot-embossing, as demonstrated in terms of free volume theory and finite element method simulation, respectively. Our findings are fundamentally useful for understanding the TPF mechanism of BMGs.

Acknowledgements

This work was financially supported by the National Nature Science Foundation of China under Grant Nos. 51005081, 51071072 and 11002144. The work was also partially supported by the funding from the State Key Laboratory for Mechanical Behavior of Materials, Xi'an Jiaotong University. The authors are grateful to the Analytical and Testing Center, Huazhong University of Science and Technology, for technical assistance.

Appendix A. Supplementary material

Supplementary data associated with this article can be found, in the online version, at http://dx.doi.org/10.1016/j.actamat.2012.12.013.

References

[1] Johnson WL. MRS-Bull 1999;24:42.
[2] Inoue A, Takeuchi A. Acta Mater 2011;59:2243.
[3] Greer AL. Science 1995;267:1947.
[4] Schuh CA, Hufnagel TC, Ramamurty U. Acta Mater 2007;55:4067.
[5] Schroers J. Adv Mater 2009;21:1.
[6] Wang WH. Adv Mater 2009;21:4524.
[7] Chen MW. Annu Rev Mater Res 2008;38:445.
[8] Spaepen F. Acta Metall 1977;25:407.
[9] Jiang WH, Fan GJ, Liu FX, Wang G, Choo H, Liaw PK. Int J Plast 2008;24:1.
[10] Jiang MQ, Ling Z, Meng JX, Dai LH. Philos Mag 2008;88:407.
[11] Jiang MQ, Dai LH. J Mech Phys Solids 2009;57:1267.
[12] Jiang MQ, Wang WH, Dai LH. Scripta Mater 2009;60:1004.
[13] Pan J, Chen Q, Liu L, Li Y. Acta Mater 2011;59:5146.
[14] Megusar J, Argon AS, Grant NJ. Mater Sci Eng 1979;38:63.
[15] Prasad YVRK, Gegel HL, Doraivelu SM, Malas JC, Morgan JT, Lark KA, et al. Metall Trans 1984;15A:1883.
[16] Schuh CA, Lund AC, Nieh TG. Acta Mater 2004;52:5879.
[17] Furukawa A, Tanaka H. Nat Mater 2009;8:601.
[18] Kawamura Y, Kato H, Inoue A, Masumoto T. Appl Phys Lett 1995;67:2008.
[19] Nishiyama N, Inoue A. Mater Trans Jim 1999;40:64.
[20] Saotome Y, Miwa S, Zhang T, Inoue A. J Mater Process Technol 2001;113:64.
[21] Saotome Y, Itoh K, Zhang T, Inoue A. Scripta Mater 2001;44:1541.
[22] Saotome Y, Iwazaki H. J Mater Process Technol 2001;119:307.
[23] Sharma P, Kaushik N, Kimura H, Saotome Y, Inoue A. Nanotechnology 2007;18:035302.
[24] Chu JP, Wijaya H, Wu CW, Tsai TR, Wei CS, Nieh TG, et al. Appl Phys Lett 2007;90:034101.
[25] Bardt JA, Bourne GR, Schmitz TL, Ziegert JC, Sawyer WG. J Mater Res 2007;22:339.
[26] Henann DL, Srivastava V, Taylor HK, Hale MR, Hardt DE, Anand L. J Micromech Microeng 2009;19:115030.
[27] Wiest A, Harmon JS, Demetriou MD, Conner RD, Johnson WL. Scripta Mater 2009;60:160.
[28] Schroers J. JOM 2005;57:35.
[29] Kumar G, Schroers J. Appl Phys Lett 2008;92:031901.
[30] Kumar G, Tang H, Schroers J. Nature 2009;457:868.
[31] Kumar G, Desai A, Schroers J. Adv Mater 2011;23:461.
[32] Sarac B, Ketkaew J, Popnoe DO, Schroers J. Adv Funct Mater 2012;22:3161.
[33] Schroers J, Pham Q, Peker A, Paton N, Curtis RV. Scripta Mater 2007;57:341.
[34] Kumar G, Staffier PA, Blawzdziewicz J, Schwarz UD, Schroers J. Appl Phys Lett 2010;97:101907.
[35] Xia T, Li N, Wu Y, Liu L. Appl Phys Lett 2012;101:081601.
[36] He JJ, Li N, Tang N, Wang XY, Zhang C, Liu L. Intermetallics 2012;21:50.
[37] Busch R, Bakke E, Johnson WL. Acta Mater 1998;46:4725.
[38] Waniuk TA, Busch R, Masuhr A, Johnson WL. Acta Mater 1998;46:5229–36.
[39] Saotome Y, Imai K, Shioda S, Shimizu S, Zhang T, Inoue A. Intermetallics 2002;10:1241.
[40] Saotome Y, Imai K, Sawanobori N. J Mater Process Technol 2001;140:379.
[41] Schroers J. Acta Mater 2008;56:471.
[42] Pitt EB, Kumar G, Schroers J. J Appl Phys 2011;110:043518.
[43] Ishida M, Takeda H, Watanabe D, Amiya K, Nishiyama N, Kita K, et al. Mater Trans 2004;45:1239.
[44] Kato H, Wada T, Hasegawa M, Saida J, Inoue A, Chen HS. Scripta Mater 2006;54:2023.
[45] Zhang W, Inoue A. Mater Trans 2003;44:2220.
[46] Waniuk T, Schroers J, Johnson WL. Phys Rev B 2003;67:184203.
[47] Mukherjee S, Schroers J, Zhou Z, Johnson WL, Rhim WK. Acta Mater 2004;52:3689–95.
[48] Kawamura Y, Nakamura T, Inoue A. Scripta Mater 1998;39:301.
[49] Lee KS, Jun HJ, Chang YW. Mater Sci Eng A 2007;449–451:941.
[50] Jun HJ, Lee KS, Chang YW. Intermetallics 2009;17:463.
[51] Mei JN, Soubeyroux JL, Blandin JJ, Li JS, Kou HC, Fu HZ, et al. Intermetallics 2011;19:48.
[52] Lee KS, Jun HJ, Kim CP, Eckert J, Chang YW. Key Eng Mater 2007;345–346:105.
[53] Ragani J, Wang Q, Gravier S, Blandinc JJ. Key Eng Mater 2010;433:345.
[54] Duan G, Wiest A, Lind ML, Li J, Rhim WK, Johnson WL. Adv Mater 2007;19:4272.
[55] Chiu HM, Kumar G, Blawzdziewicz J, Schroers J. Scripta Mater 2009;61:28.
[56] Johnson WL, Lu J, Demetriou MD. Intermetallics 2002;10:1039.
[57] Cohen MH, Grest GS. Phys Rev B 1979;20:1077.
[58] Masuhr A, Waniuk TA, Busch R, Johnson WL. Phys Rev Lett 1999;82:2290.
[59] Yang Q, Mota A, Ortiz M. Comput Mech 2006;37:194.
[60] Kawamura Y, Nakamura T, Inoue A, Masumoto T. Mater Trans JIM 1999;40:794.
[61] Van Den Beukel A, Sietsma J. Acta Metall Mater 1990;38:383.
[62] Wang XY, Tang N, Zheng ZZ, Tang YY, Li JJ, Liu L. J Alloys Compd 2011;509:2518.
[63] <http://en.wikipedia.org/wiki/Yellow_Crane_Tower>.